

University of Nebraska - Lincoln

DigitalCommons@University of Nebraska - Lincoln

Evgeny Tsybal Publications

Research Papers in Physics and Astronomy

2019

Controlling the magnetic properties of LaMnO₃/SrTiO₃ heterostructures by stoichiometry and electronic reconstruction: Atomic-scale evidence

M. S. Li, C. H. Tang, T. R. Paudel, D. S. Song, W. M. Lü, K. Han, Z. Huang, S. W. Zeng, X. R. Wang, P. Yang, Ariando, J. S. Chen, T. Venkatesan, E. Y. Tsybal, C. J. Li, and S. J. Pennycook

Follow this and additional works at: <https://digitalcommons.unl.edu/physicstsybal>



Part of the [Condensed Matter Physics Commons](#)

This Article is brought to you for free and open access by the Research Papers in Physics and Astronomy at DigitalCommons@University of Nebraska - Lincoln. It has been accepted for inclusion in Evgeny Tsybal Publications by an authorized administrator of DigitalCommons@University of Nebraska - Lincoln.

Controlling the Magnetic Properties of LaMnO₃/SrTiO₃ Heterostructures by Stoichiometry and Electronic Reconstruction: Atomic-Scale Evidence

Mengsha Li, Chunhua Tang, Tula R. Paudel, Dongsheng Song, Weiming Lü, Kun Han, Zhen Huang, Shengwei Zeng, Xiao Renshaw Wang,* Ping Yang, Ariando, Jingsheng Chen, Thirumalai Venkatesan, Evgeny Y. Tsymbal, Changjian Li,* and Stephen John Pennycook*


Interface-driven magnetic effects and phenomena associated with spin–orbit coupling and intrinsic symmetry breaking are of importance for fundamental physics and device applications. How interfaces affect the interplay between charge, spin, orbital, and lattice degrees of freedom is the key to boosting device performance. In LaMnO₃/SrTiO₃ (LMO/STO) polar–nonpolar heterostructures, electronic reconstruction leads to an antiferromagnetic to ferromagnetic transition, making them viable for spin filter applications. The interfacial electronic structure plays a critical role in the understanding of the microscopic origins of the observed magnetic phase transition, from antiferromagnetic at 5 unit cells (ucs) of LMO or below to ferromagnetic at 6 ucs or above, yet such a study is missing. Here, an atomic scale understanding of LMO/STO ambipolar ferromagnetism is offered by quantifying the interface charge distribution and performing first-principles density functional theory (DFT) calculations across this abrupt magnetic transition. It is found that the electronic reconstruction is confined within the first 3 ucs of LMO from the interface, and more importantly, it is robust against oxygen nonstoichiometry. When restoring stoichiometry, an enhanced ferromagnetic insulating state in LMO films with a thickness as thin as 2 nm (5 uc) is achieved, making LMO readily applicable as barriers in spin filters.

Charges and spins in strongly correlated systems determine the electronic and magnetic structures, which define the corresponding electronic and magnetic properties.^[1,2] Charge modulation, achieved through chemical and electrostatic doping, is a common technique to modify the band filling status. These modified electronic structures have an influence on the properties, e.g. high temperature superconductivity, electronic phase separation, and charge ordering.^[2–4] Nonstoichiometry, which commonly exists in materials, results in an unintentional doping, altering their properties.^[5] For example, oxygen-deficient SrTiO_{3–x} becomes conductive,^[6] in contrary stoichiometric SrTiO₃ (STO) is a typical band insulator with a band gap of 3.2 eV. In manganite-,^[7,8] cobalt-,^[9,10] iron-, and nickel-based perovskites,^[11,12] the nonstoichiometry of oxygen not only introduces electron/hole doping but also affects the super-exchange or double-exchange interactions by modification of

M. Li, Dr. C. Tang, Prof. J. Chen, Dr. C. Li, Prof. S. J. Pennycook
Department of Materials Science and Engineering
National University of Singapore
Singapore 117575, Singapore
E-mail: mselc@nus.edu.sg; steve.pennycook@nus.edu.sg

Prof. T. R. Paudel, Prof. E. Y. Tsymbal
Department of Physics and Astronomy and Nebraska
Center for Materials and Nanoscience
University of Nebraska
Lincoln, NE 68588, USA

Dr. D. Song, Dr. K. Han, Dr. Z. Huang, Dr. S. Zeng, Prof. Ariando,
Prof. T. Venkatesan, Prof. S. J. Pennycook
NUSNNI-Nanocore
National University of Singapore
Singapore 117411, Singapore

 The ORCID identification number(s) for the author(s) of this article can be found under <https://doi.org/10.1002/adma.201901386>.

DOI: 10.1002/adma.201901386

Prof. W. Lü
Spintronics Institute
University of Jinan
Jinan 250022, China

Prof. W. Lü
Condensed Matter Science and Technology Institute
and Department of Physics
Harbin Institute of Technology
Harbin 150001, China

Prof. X. Renshaw Wang
School of Physical and Mathematical Sciences and School of Electrical
and Electronic Engineering
Nanyang Technological University
Singapore 639798, Singapore
E-mail: rensshaw@ntu.edu.sg

Dr. P. Yang
Singapore Synchrotron Light Source National University of Singapore
5 Research Link
Singapore 117603, Singapore

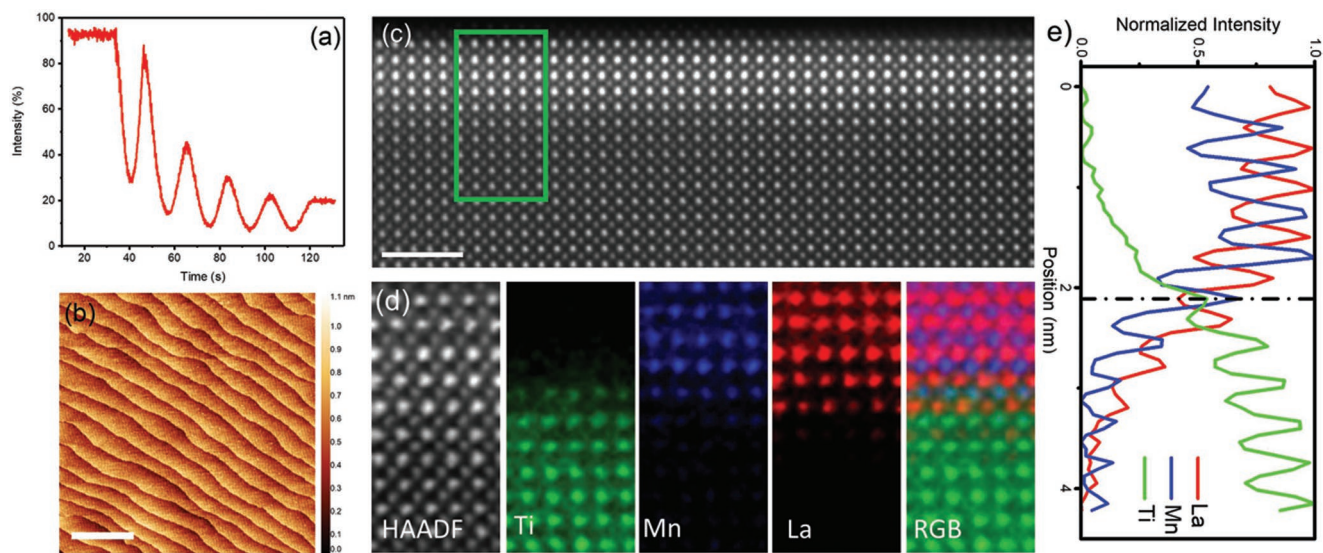


Figure 1. Fabrication and structural characterization of the LMO/STO heterostructures. a) A RHEED intensity oscillation curve and b) an AFM topography image of a 5 uc LMO film grown on a STO substrate. c) Corresponding cross-sectional HAADF-STEM images and d) simultaneously acquired HAADF and EELS elemental mappings (Ti, Mn, La, and RGB mix) from the green box in (c). e) The line intensity profile for Ti, Mn, and La across the LMO/STO interface, the dashed line indicating the position of the interface. The scale bars in the AFM and HAADF images are 1 μm and 2 nm, respectively.

the metal–oxygen bond length and/or angle.^[13] One example is oxygen-deficient LaCoO_{3-x} which becomes a ferromagnetic (FM) insulator via modification of Co spin states,^[14] while stoichiometric LaCoO_3 is antiferromagnetic (AFM).

The arrangement of charge within a specific lattice structure determines the macroscopic polarity.^[15,16] For example, in ABO_3 perovskite oxides, the alternating stacking of AO^+ and BO_2^- layers makes them polar when both A and B cations are trivalent. Within heterostructures, a polarity mismatch occurs at a polar–nonpolar interface (e.g., a LaAlO_3 (LAO)/STO interface). Such an electrostatic discontinuity can drive an electronic/atomic reconstruction.^[15–18] In real material systems, nonstoichiometry can coexist with polarity mismatch,^[19] but how they interact with each other and affect the electronic and magnetic properties is still unclear.^[20–22] Therefore, a quantitative description of the interaction between nonstoichiometry and polar mismatch at the atomic level is essential to achieve better electronic and spintronic devices.^[23,24]

One of the best systems for this study is LaMnO_3 (LMO)/STO heterostructures. LMO is an antiferromagnetic insulator in bulk form,^[25,26] however, with moderate doping, it becomes a ferromagnetic insulator.^[2,7,27] It is a good candidate for spin filter applications for its simple perovskite structure and relatively high T_c compared to conventional ferromagnetic insulators (e.g., EuS , NiFe_2O_4 , and CoFe_2O_4).^[28–30] Along the [001] direction, LMO is a polar oxide due to the alternating charged $(\text{LaO})^+$ and $(\text{MnO}_2)^-$ layers while STO is nonpolar. The polar discontinuity at the LMO/STO interface induces an electronic reconstruction, which drives the AFM to FM transition via electron doping.^[31] In addition, LMO tends to contain excess oxygen δ ($\text{LaMnO}_{3+\delta}$). Since oxygen cannot stay in the interstitial sites, excess oxygen is realized by cation vacancies, in the form of $\text{La}_{1-\varepsilon}\text{Mn}_{1-\varepsilon}\text{O}_3$ (Figure S1, Supporting Information), where $\varepsilon = \delta/(3 + \delta)$.^[32] The excess oxygen (in the form of cation

vacancies) leads to a partial oxidation from Mn^{3+} to Mn^{4+} and hence ferromagnetism is favored due to double exchange in the mixed $\text{Mn}^{3+}/\text{Mn}^{4+}$ system via hole doping.^[32,33] In the LMO/STO heterostructures, we therefore expect that both origins coexist and probably correlated. Disentangling the two different origins for the observed ferromagnetic insulating properties in LMO/STO heterostructures remains an interesting and challenging problem.

Here, we provide an atomic-scale picture of the coexistence of nonstoichiometry and electronic reconstruction at the LMO/STO interface using atomic-resolution scanning transmission electron microscopy (STEM) and electron energy loss spectroscopy (EELS), and further validate this picture with DFT calculations. We show that electronic reconstruction is restricted to only 3 unit cells (ucs) inside the LMO from the LMO/STO interface. We tune the oxygen stoichiometry by a vacuum annealing treatment, and successfully reduce the critical thickness for electronic reconstruction from 6 to 5 ucs, which is consistent with the DFT calculations. Furthermore, the ferromagnetic insulating properties of LMO are significantly enhanced at a thickness of only 5 uc (≈ 2 nm), making it possible to construct efficient and reliable spin filters.

Figure 1a shows the reflection high energy electron diffraction (RHEED) intensity oscillations obtained during a 5 uc-LMO growing on an STO substrate. It suggests a layer-by-layer growth mode, consistent with the atomic-terrace topography observed by atomic force microscopy (AFM), as shown in Figure 1b. An atomically sharp LMO/STO interface is observed in a high angle annular dark field (HAADF)-STEM image (Figure 1c). Clearly, the LMO film, perfectly epitaxially grown on the STO, shows minimal defects and is fully strained. In addition, atomic-resolution EELS elemental mappings of La, Mn, and Ti are summarized in Figure 1d. The apparent interdiffusion is limited to 1 uc, which further confirms the sharp

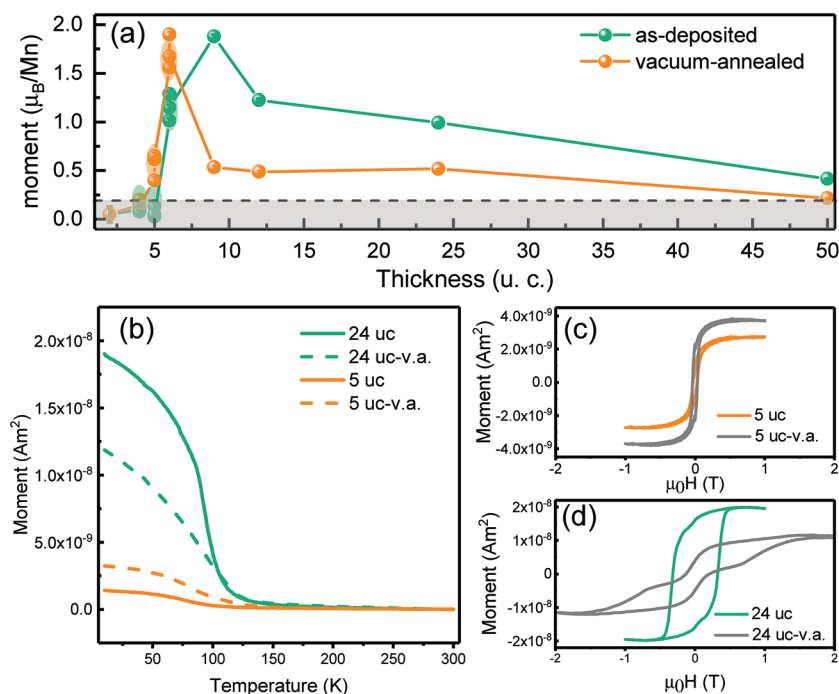


Figure 2. Magnetic properties of the LMO/STO heterostructures with different LMO thicknesses before and after vacuum annealing. a) Normalized in-plane magnetic moment (measured at 10 K) as a function of the LMO film thickness for the samples before and after vacuum annealing. Multiple data points are presented for the 4, 5, and 6 uc samples near the magnetic phase transition region. The gray shaded area denotes the moment below the threshold of $0.2 \mu_B/\text{Mn}$, which is the canted moment of stoichiometric LMO. b) Temperature-dependent magnetic moment of 5 and 24 uc as-deposited (solid lines) and vacuum annealed (dashed lines) samples, respectively. The cooling field is 1 T and measurement field is 0.1 T. c,d) Magnetic hysteresis loops (measured at 10 K) of 5 and 24 as-deposited and vacuum annealed samples, respectively.

interface across the heterostructure. Additional AFM and high-resolution X-ray diffraction (HRXRD) data confirm the good quality of the films on a macroscopic scale (Figures S2 and S3 of the Supporting Information, respectively).

Figure 2a shows the thickness-dependent in-plane magnetic moment, normalized by Mn atoms, measured at 10 K by a superconducting quantum interference device-vibrating sample magnetometer (SQUID-VSM). The transition from AFM to FM happens in as-deposited LMO/STO heterostructures with thickness from 5 to 6 uc, in agreement with previous findings.^[31,34] To eliminate the excess oxygen in the LMO, the LMO/STO heterostructures, with LMO thickness from 4 to 50 ucs, were annealed at 1×10^{-6} Torr and 700 °C for 2 h. For simplicity, we name the LMO/STO heterostructures with LMO thickness of t ucs before and after vacuum annealing as “ t uc” sample and “ t uc-v.a.” samples, respectively. In these vacuum-annealed samples, the magnetic moment is suppressed at the higher thicknesses but enhanced when the LMO thickness is in the region of 4 to 6 ucs. Taking the 5 uc sample as an example, the magnetic moment increases from 0.2 to $0.4 \mu_B/\text{Mn}$ at 10 K with the help of vacuum annealing, as shown both in the magnetic moment versus temperature curve (M - T curve, Figure 2b) and the magnetic hysteresis loop (Figure 2c). From the M - T curve, the Curie temperature (T_c) remains the same after vacuum annealing. At the LMO thickness of 24 ucs, the magnetic

moment decreases from 1.1 to $0.4 \mu_B/\text{Mn}$ after vacuum annealing (Figure 2a), while T_c also remains the same (≈ 100 K in Figure 2b). When the LMO thickness increases to 50 ucs, the magnetic moment is suppressed down to $\approx 0.22 \mu_B/\text{Mn}$, being very close to the canted moment ($\approx 0.2 \mu_B/\text{Mn}$) of the bulk LMO antiferromagnetic state.^[25] Moreover, when we further extend the vacuum annealing duration to 4 h, the magnetic moments remain the same as the 2 h annealing results (Figure S4, Supporting Information). It means that a fully stoichiometric LMO state has been recovered after a 2 h vacuum annealing, confirming that excess oxygen exists in the as-deposited films. Therefore, the as-deposited films can be denoted as $\text{LMO}_{3+\delta}$, where δ is estimated to be 0.1 from the magnetic moment changes via the vacuum annealing, as the moment and T_c values are comparable with previous studies on magnetic properties of $\text{LMO}_{3.1}$.^[35] This oxygen-excess state for as-deposited samples is also confirmed by the HRXRD results. Previous studies show that the $\text{LMO}_{3+\delta}$ cell volume decreases almost linearly with the value of δ .^[36,37] We observe an expansion in lattice constant c in vacuum annealed samples, meaning the cell volume increases (Figure S3, Supporting Information). The cell volume expansion indicates that the nonstoichiometric δ is reduced after vacuum annealing.

To investigate possible changes in atomic or electronic structure after vacuum annealing, we performed HAADF-STEM and EELS spectrum imaging on the 5, 6, and 24 uc samples, before and after vacuum annealing. We could not identify any structural changes from the HAADF images (see Figure S5, Supporting Information). The difference lies in the electronic state of Mn due to the vacuum annealing. Figure 3a, c, and e present a series of uc-by-uc Mn- $L_{2,3}$ edge spectra across the LMO/STO interfaces of 5, 6, and 24 uc as-deposited films, respectively. (For the purpose of clarity, only selected spectra are presented after the third uc). For the 5 uc sample, all Mn- L_3 peaks are located at ≈ 641.1 eV, indicating the same Mn valence throughout the film. In contrast, the 6 uc sample exhibits a red shift of 0.40 eV in the first 2 ucs from the interface, whereas the L_3 peaks are at 641.5 eV for the rest of the MnO_2 layers. This red shift indicates the Mn valence changes from Mn^{3+} to Mn^{2+} due to extra electrons, which are attributed to the electronic reconstruction caused by the polar discontinuity. A similar red shift appears in the first 2 ucs next to the interface in the 24 uc samples. Therefore, the electronic reconstruction arises in the as-deposited samples with an LMO thickness of 6 ucs and above. For comparison, Figure 3b, d, and f present the Mn EEL spectra of the vacuum-annealed 5, 6, and 24 uc samples, respectively. In the 5 uc vacuum-annealed sample, a red shift of Mn EEL spectra compared to the as-deposited sample is seen in the first 2 ucs of LMO. When LMO films of 6 ucs and above are

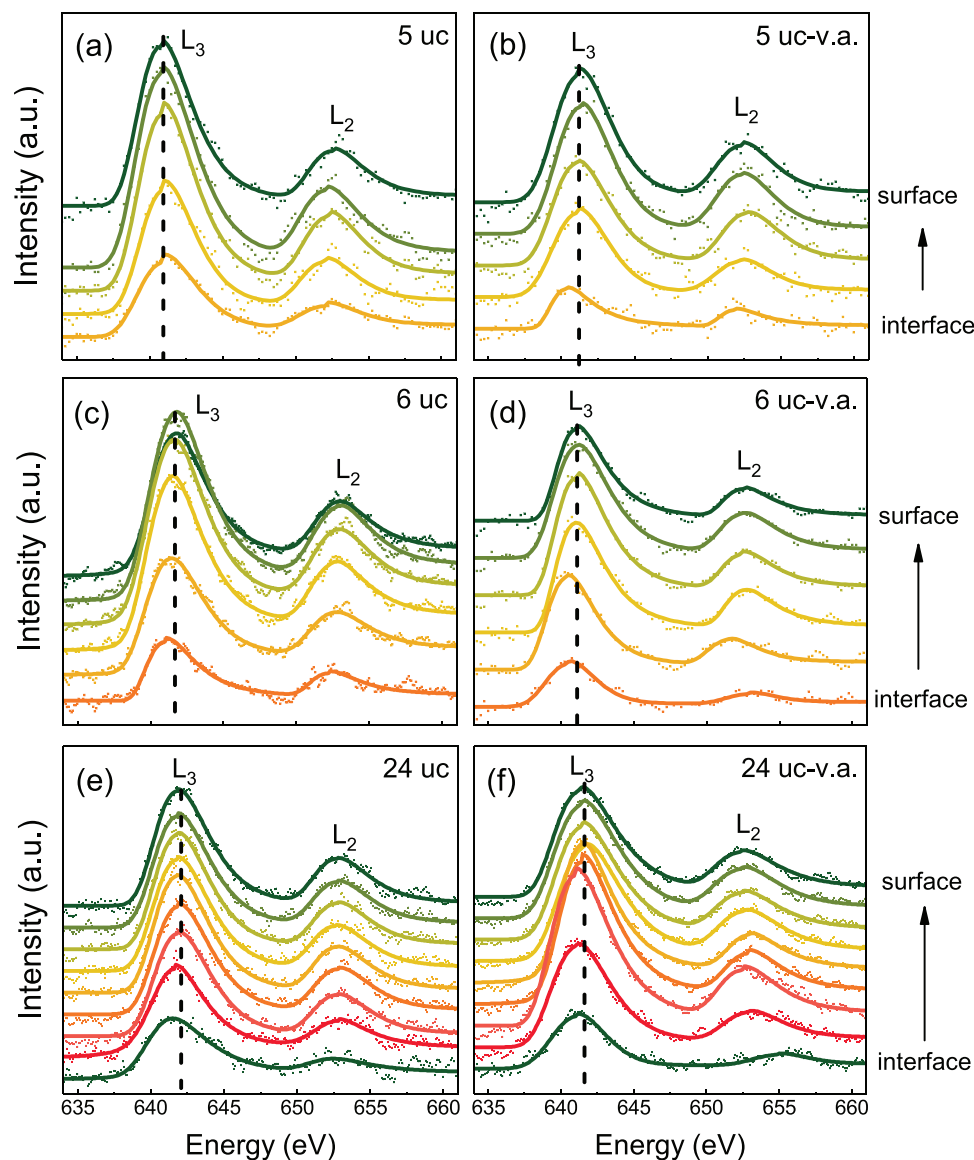


Figure 3. a–f) Electronic doping at the LMO/STO interface revealed by STEM-EELS. uc-by-uc Mn- $L_{2,3}$ EEL spectra across the LMO/STO interfaces of 5, 6, and 24 uc samples before (a,c,e) and after (b,d,f) vacuum annealing. The dashed lines are guides to the bulk Mn- L_3 peak position.

vacuum-annealed, the red shift remains the same. It proves that the electronic reconstruction starts from 5 uc, instead of 6 uc, after vacuum annealing. The decrease in the critical thickness proves that vacuum annealing, which results in a change in the oxygen stoichiometry, has a direct influence on the electronic reconstruction. In addition, for samples with an LMO thickness of 6 uc and above, the electronic reconstruction is robust against a degree of nonstoichiometry.

To quantitatively analyze the Mn EEL spectra, we extract the L_3 peaks and calculate the L_3/L_2 white-line intensity ratios to identify the Mn electronic configuration uc-by-uc. In an Mn EEL spectrum, L_3 and L_2 peaks correspond to $2p_{3/2} \rightarrow 3d$ and $2p_{1/2} \rightarrow 3d$ transitions, respectively. Therefore, the L_3/L_2 area ratio is sensitive to the number of electrons in the Mn 3d orbital, thus offering a useful method to determine the local Mn valence in the LMO films. The L_3/L_2 white-line ratio was calculated from a

fitting by a combination of Gaussian and Lorentzian functions sitting on a step function, after a power-law background subtraction (Figure S6, Supporting Information).^[38]

Figure 4a shows the L_3/L_2 ratios and L_3 peak positions for the 5, 6, and 24 uc samples before vacuum annealing. Three dashed lines represent the L_3/L_2 ratios for pure Mn^{2+} , Mn^{3+} , and Mn^{4+} states (4.2 for Mn^{2+} , 3.0 for Mn^{3+} , and 2.0 for Mn^{4+}), which are obtained from ref. [39], our pulsed laser deposition (PLD) deposited thick LMO film after vacuum annealing and $CaMnO_3$ film as reference samples,^[40] respectively. For the 5 uc sample, the L_3/L_2 ratios for all MnO_2 layers are about 2.9; and all the L_3 peak positions remain at about 641.1 eV, proving negligible transferred electrons. When the LMO thickness increases to 6 ucs, the L_3/L_2 ratios increase to 3.1 in the first 2 ucs near the LMO/STO interface and then drop to 2.9 onward. Meanwhile, the L_3 peak shifts from 641.0 (first uc) to 641.3 eV

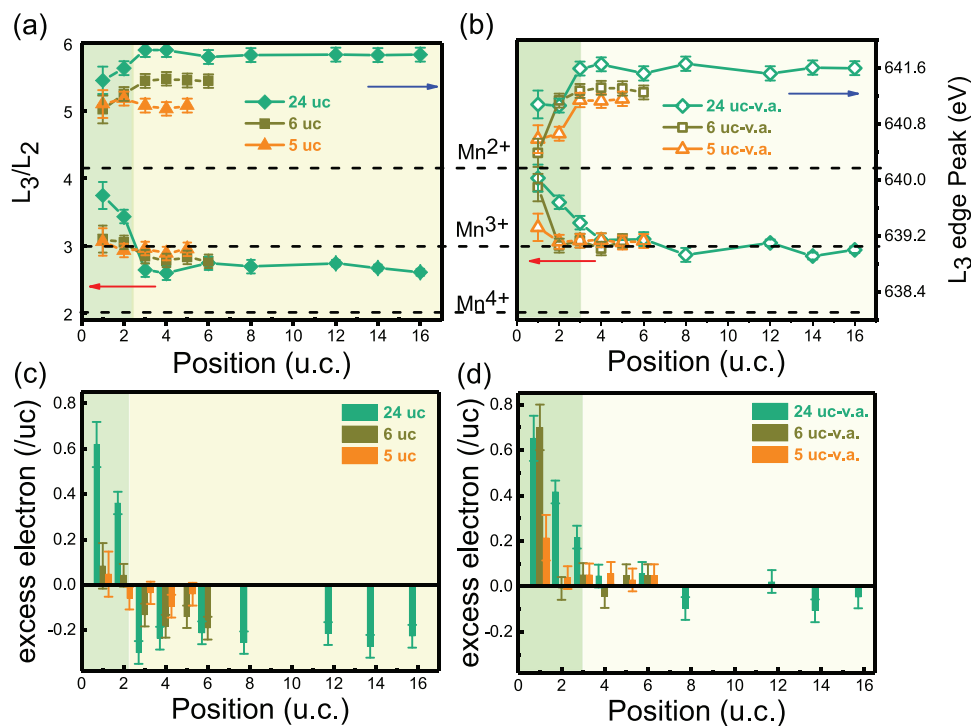


Figure 4. Quantification of electron and hole doping in the LMO/STO heterostructures. a,b) uc-by-uc Mn- L_3/L_2 area ratios and L_3 peak positions of 5, 6, and 24 uc samples before and after vacuum annealing, respectively. The three dashed lines represent the reference Mn- L_3/L_2 area ratios for Mn^{2+} , Mn^{3+} , and Mn^{4+} . c,d) Calculated excess electrons from Mn- L_3/L_2 area ratios of 5, 6, and 24 uc samples before and after vacuum annealing, respectively. The green and yellow shaded areas indicate the electron and hole doped regions of the LMO film, respectively.

(second uc) and saturates at 641.5 eV for the remaining ucs. Using a linear approximation of the L_3/L_2 ratio dependence on Mn valence, we calculate the number of excess charges, relative to Mn^{3+} , for all the samples. In Figure 4c, there are less than 0.05 excess e^- per uc in the entire 5 uc as-deposited LMO film. When it comes to the 6 uc sample, $\approx 0.15 e^-$ per uc are present within the first 2 ucs near the interface which are regarded as the electron doped region. Then, the region from the third uc, in which the L_3/L_2 area ratios are slightly less than 3 (a Mn^{3+}/Mn^{4+} mixed valence state), is hole doped. The excess charges are denoted as negative values (≈ 0.22 hole per uc from the third uc onward). The same trends in the L_3/L_2 ratios and L_3 peak positions are observed in the 24 uc sample, with excess charges in the electron-doped (0.6 and $0.3 e^-$ per uc for the first and second uc, respectively) and hole-doped (≈ 0.22 hole per uc from the third uc onward) regions. It is noteworthy that the 0.22 hole per uc is consistent with the previous estimated excess oxygen ($\delta = 0.1$), which contributes to the hole doping of 0.2 hole per uc. Figure 4b shows the L_3/L_2 ratios and L_3 peak positions of all vacuum-annealed samples. Compared with the samples before vacuum annealing, the electron doping is enhanced in the first 2 ucs near the interfaces (the green region), evidenced by large L_3/L_2 ratios (close to 3.9 for 6 and 24 uc vacuum-annealed samples). Moreover, from the third uc onward (the yellow region), the L_3/L_2 ratios increase slightly and saturate at about 3.0, which correspond to the pure Mn^{3+} state. Meanwhile, the L_3 peak positions also shift to the lower values, which is consistent with the reduction of Mn valence by vacuum annealing. In the excess charge plot (Figure 4d), the electron doping within the

first 2 ucs (3 ucs for the 24-v.a. sample) is enhanced while the hole doping (the yellow region) is eliminated. In addition, for the 24 uc and 24 uc-v.a. samples, uc-by-uc O K edge EEL spectra (Figure S7, Supporting Information) prepeaks show interfacial electron doping and bulk hole doping that are fully consistent with the Mn EEL spectra analysis.

Intermixing could also have a major effect on the Mn electronic state. Apparently, in the EELS mapping (Figure 1d), the intermixing is limited to 1 uc across the interface which can be written as $(La,Sr)(Ti,Mn)O_3$. However, the Ti valence remains 4+ throughout the STO substrate for the 24 uc sample, even near the interface (Figure S8, Supporting Information), in agreement with the previous reported X-ray absorption spectroscopy and EELS measurements.^[41,42] To preserve charge neutrality, the valence of Mn in the intermixed region should increase from Mn^{3+} to Mn^{4+} , opposite to our experimental observations. Therefore, the apparent intermixing is possibly due to the broadening of the electron probe as it propagates through the sample. Such lateral spreading causes an atomically abrupt interface to appear interdiffused.^[43] From the atomic scale valence information of Ti and Mn, we gain a clear understanding of the role of electronic reconstruction on forming a ferromagnetic insulating interface (the insulating transport behavior shown in Figure S10 of the Supporting Information) rather than a conducting interface as in LMO-STO heterostructures. This scenario is different from the case of the LAO/STO interface since LMO has a smaller bandgap (1.1 eV) than STO (3.2 eV), whereas LAO has a larger bandgap (5.6 eV). Therefore, the transferred electrons exist in the conduction band of LMO,

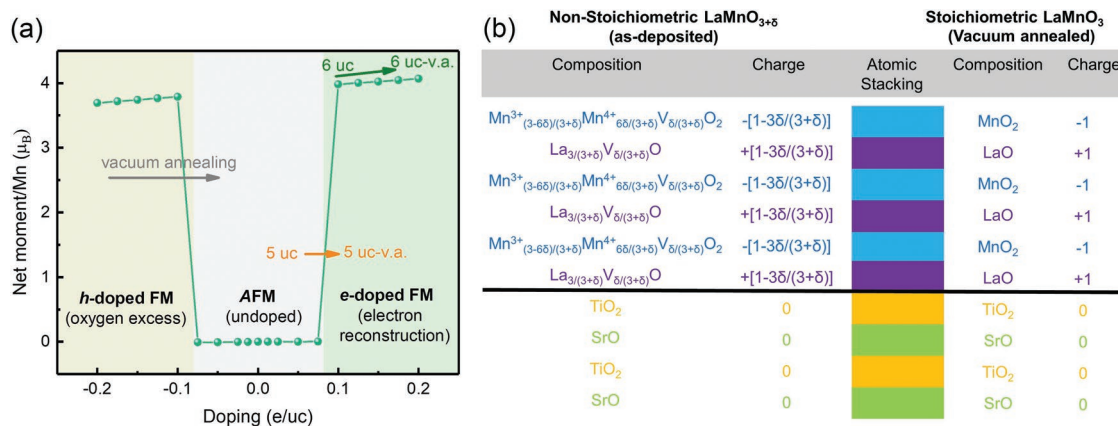


Figure 5. Stoichiometry and electronic reconstructions as origins of ferromagnetism in LMO/STO heterostructures. a) DFT calculated net magnetic moments as a function of electron doping in biaxially strained LMO, showing an e-doped FM region and a h-doped region when the doping concentration is above 0.1 e/h per uc. The gray arrow represents that vacuum annealing reduces hole doping for all film thicknesses, while orange and olive colored arrows represent the change in e-doping for 5 and 6 uc samples. b) Schematic representing the atomic stacking order of as-deposited and vacuum annealed LMO. Due to the presence of excess oxygen, δ , or the equivalent cation vacancies, the formal charge reduces from ± 1 to $\pm 1 - [3\delta/(3 + \delta)]$, leading to a smaller driving force for the electronic reconstruction.

instead of $\text{STO}^{[31]}$; the schematic electron reconstruction is shown in Figure S9 (Supporting Information).

The magnetic properties of LMO are determined by the Mn spin exchange interactions within the perovskite lattice. In the stoichiometric LMO, Mn^{3+} is a Jahn-Teller ion with a $t_{2g}^3e_g^1$ occupancy, which creates a ground state of an A-type AFM state, where the in-plane interaction is ferromagnetic while the out-of-plane interaction is AFM.^[26] When it is doped either by electrons (both e_g orbitals half-filled as $t_{2g}^3e_g^2$ for Mn^{2+}) or holes (empty e_g orbitals as $t_{2g}^3e_g^0$ for Mn^{4+}), the local environment around Mn^{3+} ions becomes more isotropic, which increases the ferromagnetic interaction between quarter filled e_g orbitals and reduces the antiferromagnetic super exchange interaction between half-filled t_{2g} orbitals. **Figure 5a** shows the calculated net magnetic moment of Mn as a function of electron and hole doping concentration in a biaxially strained LMO film on an STO substrate. When the doping concentration is low (less than 0.1 e per uc or 0.1 hole per uc), the LMO remains in the AFM state. Once the doping surpasses the threshold, the net moment increases suddenly because the FM state is energetically favored. This increase of the net moment with electron/hole doping is consistent with earlier experiments.^[27,44,45]

In our system, the electron-doping comes from the electronic reconstruction while hole-doping comes from the excess oxygen. The former is an interfacial phenomenon while the latter is present in the entire film. Hence, we expect the electronic reconstruction to dominate magnetic properties in the thin (no more than 6 ucs) LMO films but the latter for thick films (larger than 6 ucs). Because the excess oxygen ($\delta = 0.1$) in the LMO film is eliminated via vacuum annealing, the hole doping reduces from 0.2 to 0 hole per uc, and it induces a transition from FM to AFM (gray arrow for all thickness samples in Figure 5a). Only a small moment $\approx 0.2 \mu_B/\text{Mn}$ is observed in the stoichiometric LMO film originating from the Dzyaloshinskii–Moriya interaction,^[35] as shown in the 50 uc-v.a. sample.

Oxygen stoichiometry determines the polar effective charge thus the electronic reconstruction induced FM. Schematics of

the LMO and $\text{LMO}_{3+\delta}$ structures are illustrated in Figure 5b. The alternating charged layers of $(\text{LaO})^+$ and $(\text{MnO}_2)^-$ in the stoichiometric LMO films have +1 and -1 polar charges, respectively. The $\text{LMO}_{3+\delta}$ films can be written in the form $\text{LaMn}_{2\delta}^{4+}\text{Mn}_{(1-2\delta)}^{3+}\text{O}_{3+\delta}$ to account for the emergence of Mn^{4+} . Furthermore, to account for equal number of La and Mn vacancies, we write^[32]

$$\text{LaMn}_{2\delta}^{4+}\text{Mn}_{1-2\delta}^{3+}\text{O}_{3+\delta} = \frac{3+\delta}{3} \left[\text{La}_{\frac{3}{3+\delta}} \text{V}_{\frac{\delta}{3+\delta}} \text{Mn}_{\frac{6\delta}{3+\delta}}^{4+} \text{Mn}_{\frac{3-6\delta}{3+\delta}}^{3+} \text{V}_{\frac{\delta}{3+\delta}} \text{O}_3 \right] \quad (1)$$

where the charged sheets change to $(\text{La}_{3/(3+\delta)}\text{V}_{\delta/(3+\delta)}\text{O})$ and $(\text{Mn}_{6\delta/(3+\delta)}^{4+}\text{Mn}_{(3-6\delta)/(3+\delta)}^{3+} \text{V}_{\delta/(3+\delta)}\text{O}_2)$, with charges of $+[1-3\delta/(3+\delta)]$ and $-[1-3\delta/(3+\delta)]$. Here δ is 0.1, and the effective polar charge $Q_{\text{eff}} = \{1 - [3\delta/(3+\delta)]\} = 0.903$, about 90% of the stoichiometric value. As in the LAO/STO system,^[46,47] the effective polar charge determines: 1) the critical thickness initiating the electronic reconstruction and 2) the number of transferred electrons at the LMO/STO interface. 1) The critical thickness $t_c = E_{g(\text{LMO})}/E_0$, where $E_{g(\text{LMO})}$ is the bandgap of LMO (≈ 1.1 eV) and E_0 is the internal electric field. More specifically, $E_0 = eQ_{\text{eff}}/[2A\epsilon_0\epsilon_r(\text{LMO})]$, where Q_{eff} is the effective polar charge, e is the elemental charge, A is the unit cell area, ϵ_0 and $\epsilon_r(\text{LMO})$ are permittivity of the vacuum and relative permittivity of the LMO film, respectively. Hence, t_c is inversely proportional to the effective polar charge, i.e., $t_c = [2A\epsilon_0\epsilon_r(\text{LMO})E_{g(\text{LMO})}]/eQ_{\text{eff}}$, assuming the change in the LMO relative permittivity and bandgap is negligible. With vacuum annealing, Q_{eff} becomes 1 instead of 0.903. Therefore, the critical thickness reduces from 6 to 5 ucs. It corresponds to the e-doping concentration increasing beyond 0.1 e per uc in the 5 uc-v.a. sample (orange arrow in Figure 5a), which stabilizes the FM phase. 2) The effect of Q_{eff} on the number of the transferred electrons is also very straightforward; $n(t) = 0.5eQ_{\text{eff}}(1 - t_c/t) = 0.5eQ_{\text{eff}} - [A\epsilon_0\epsilon_r(\text{LMO})E_{g(\text{LMO})}]/t$, where n is the number of transferred electrons at an LMO thickness of t with a critical thickness of t_c . Hence, $n(6 - \text{v.a.})$ is enhanced as Q_{eff} turns into 1 compared to the as-deposited samples (0.903).

This enhanced ϵ -doping results in a larger magnetic moment because the moment increases monotonically with electron-doping, as described by the olive colored arrow in Figure 5a. When we consider the vacuum annealing effects on thin (5 and 6 ucs) LMO samples, the increased moment is due to the enhanced electronic reconstruction, since the hole-doped ferromagnetism (originated from oxygen excess) is eliminated.

In summary, both electronic reconstruction and oxygen nonstoichiometry control the magnetic properties of LMO/STO heterostructures. From the atomic resolution STEM-EELS analysis of the Mn and Ti electronic structures on as-deposited and vacuum annealed samples, with a range of LMO thicknesses, we find that electronic reconstruction induces an electron-doped ferromagnetic interface (up to 3 ucs of LMO from the interface) and that excess oxygen results in a hole-doped ferromagnetic state in the bulk of the LMO film. The oxygen nonstoichiometry determines the effective polar charge which is a crucial parameter for electronic reconstruction. Applying this principle, we successfully reduce the magnetic transition critical thickness to 5 uc by removing excess oxygen in LMO via vacuum annealing. The enhanced ferromagnetic insulating properties in our ultrathin LMO films make them suitable for tunnel barriers in spin filter devices.

Experimental Section

Sample Fabrication and Magnetic Properties Characterization: The LMO thin films were fabricated by PLD with in situ RHEED, deposited on TiO₂-terminated 5 (L) × 5 (W) × 0.5 (H) mm³ STO (001) substrates from a sintered LMO target. The growth temperature and oxygen pressure were 750 °C and 10 mTorr, respectively, adopted from previous studies.^[31] The laser fluence energy density was kept at 1.8 J cm⁻². After deposition, all samples were cooled down to room temperature with a cooling rate of 10 °C min⁻¹. The oxygen pressure was unchanged during the whole process. As-deposited LMO/STO heterostructures were directly used to perform STEM-EELS characterization and to measure the magnetic properties by a SQUID-VSM system (Quantum Design). Then the samples were annealed under a vacuum of less than 1 × 10⁻⁶ Torr at 700 °C for 2 h, these samples were called vacuum annealed samples. Then STEM-EELS and magnetic characterizations were carried out using the same parameters as the as-prepared samples. The magnetic moments of all samples were measured from room temperature to 10K with in-plane configuration.

STEM Imaging and EELS Analysis: The cross-section TEM samples were prepared by an FIB (focused ion beam) system (FEI Versa 3D) with 30 kV Ga ions, followed by a low-voltage (i.e., 2 kV) cleaning step. HAADF-STEM imaging was performed by a JEM-ARM200F (JEOL) microscope equipped with an ASCOR aberration corrector, a cold-field emission gun and a Gatan Quantum ER spectrometer, operated at 200 kV. The HAADF-STEM images were acquired using collection of the inner and outer semiangles of 68 and 280 mrad, respectively, with a beam convergent angle of 30 mrad. The EELS results were recorded using a collection angle of 100 mrad with the energy dispersion of 0.25 and 0.1 eV per channel for the elemental mapping and energy loss near edge structure (ELNES), respectively.

Computational Methods: Theoretical modeling of the orthorhombic *Pbnm* LMO was performed using density functional theory, the projected augmented wave method, and PBEsol pseudopotentials,^[48] as implemented in the Vienna ab initio simulation package.^[49] Correlation effects beyond generalized gradient approximation (GGA) were treated at a semiempirical GGA+U level within a rotationally invariant formalism with $U = 5$ eV on Mn 3d orbitals.^[50] We used 340 eV kinetic energy cutoff and 7 × 7 × 5k points for Brillouin zone integration. Calculations were performed using a $\sqrt{2} \times \sqrt{2} \times 2$ pseudocubic unit cell, which contains 20 atoms. To simulate epitaxial growth of LMO on STO (001) substrate, the in-plane pseudocubic

lattice constant was constrained to the theoretical lattice constant of STO, which was found to be $a = b = 3.90$ Å. The out-of-plane lattice constant c and all internal atomic coordinates were fully relaxed for each doping level and magnetic configuration, using the force convergence limit of 1 meV per atom. The constraint of the in-plane lattice constant led to LMO being biaxially compressed by about 2%, resulting in $b/a = 1$ and $c/a = 1.41$, as compared to the bulk values of $b/a = 1.03$ and $c/a = 1.39$. The bipolar doping of LMO was performed by adding electrons /holes to the system and neutralizing the total charge by jellium background.

Supporting Information

Supporting Information is available from the Wiley Online Library or from the author.

Acknowledgements

M.L. and C.T. contributed equally to this work. The authors thank Prof. J. M. D. Coey for discussion on the experimental results. This work is supported by the Lee Kuan Yew Postdoctoral Fellowship through a Singapore Ministry of Education Tier 1 (Grant R-284-000-158-114). X.R.W. acknowledges support from the Nanyang Assistant Professorship grant from Nanyang Technological University and Academic Research Fund Tier 1 (RG108/17 and RG177/18) and Tier 3 (MOE2018-T3-1-002) from the Singapore Ministry of Education. S.J.P. acknowledges support from the National University of Singapore and the Ministry of Education under its Tier 2 Grant (MOE2017-T2-1-129). A.A. acknowledges the support from NUS Academic Research Fund (No. R-144-000-391-114 and No. R-144-000-403-114) and the Singapore National Research Foundation (NRF) under the Competitive Research Programs (CRP Grant No. NRF-CRP15-2015-01).

Conflict of Interest

The authors declare no conflict of interest.

Keywords

electronic reconstruction, ferromagnetic insulators, STEM-EELS, stoichiometry

Received: March 1, 2019

Revised: April 10, 2019

Published online:

- [1] M. S. Senn, J. P. Wright, J. P. Attfield, *Nature* **2012**, *481*, 173.
- [2] M. B. Salamon, M. Jaime, *Rev. Mod. Phys.* **2001**, *73*, 583.
- [3] P. A. Lee, N. Nagaosa, X.-G. Wen, *Rev. Mod. Phys.* **2006**, *78*, 17.
- [4] K. Ueno, S. Nakamura, H. Shimotani, H. T. Yuan, N. Kimura, T. Nojima, H. Aoki, Y. Iwasa, M. Kawasaki, *Nat. Nanotechnol.* **2011**, *6*, 408.
- [5] J. Jeong, N. Aetukuri, T. Graf, T. D. Schladt, M. G. Samant, S. S. P. Parkin, *Science* **2013**, *339*, 1402.
- [6] J. F. Schooley, W. R. Hosler, M. L. Cohen, *Phys. Rev. Lett.* **1964**, *12*, 474.
- [7] M. Gibert, P. Zubko, R. Scherwitzl, J. Íñiguez, J.-M. Triscone, *Nat. Mater.* **2012**, *11*, 195.
- [8] M. Gibert, M. Viret, A. Torres-Pardo, C. Piamonteze, P. Zubko, N. Jaouen, J. M. Tonnerre, A. Mougin, J. Fowlie, S. Catalan, A. Gloter, O. Stéphan, J. M. Triscone, *Nano Lett.* **2015**, *15*, 7355.

- [9] N. Lu, P. Zhang, Q. Zhang, R. Qiao, Q. He, H.-B. Li, Y. Wang, J. Guo, D. Zhang, Z. Duan, Z. Li, M. Wang, S. Yang, M. Yan, E. Arenholz, S. Zhou, W. Yang, L. Gu, C.-W. Nan, J. Wu, Y. Tokura, P. Yu, *Nature* **2017**, *546*, 124.
- [10] Q. Zhang, X. He, J. Shi, N. Lu, H. Li, Q. Yu, Z. Zhang, L.-Q. Chen, B. Morris, Q. Xu, P. Yu, L. Gu, K. Jin, C.-W. Nan, *Nat. Commun.* **2017**, *8*, 104.
- [11] R. J. Sichel-Tissot, R. C. Devlin, P. J. Ryan, J.-W. Kim, S. J. May, *Appl. Phys. Lett.* **2013**, *103*, 212905.
- [12] J. Shi, S. D. Ha, Y. Zhou, F. Schoofs, S. Ramanathan, *Nat. Commun.* **2013**, *4*, 2676.
- [13] M. Huijben, L. W. Martin, Y. H. Chu, M. B. Holcomb, P. Yu, G. Rijnders, D. H. A. Blank, R. Ramesh, *Phys. Rev. B* **2008**, *78*, 094413.
- [14] N. Biškup, J. Salafranca, V. Mehta, M. P. Oxley, Y. Suzuki, S. J. Pennycook, S. T. Pantelides, M. Varela, *Phys. Rev. Lett.* **2014**, *112*, 087202.
- [15] W. A. Harrison, E. A. Kraut, J. R. Waldrop, R. W. Grant, *Phys. Rev. B* **1978**, *18*, 4402.
- [16] H. Kroemer, *J. Cryst. Growth* **1987**, *81*, 193.
- [17] A. Ohtomo, H. Y. Hwang, *Nature* **2004**, *427*, 423.
- [18] N. Nakagawa, H. Y. Hwang, D. A. Muller, *Nat. Mater.* **2006**, *5*, 204.
- [19] C. F. Chang, Z. Hu, S. Klein, X. H. Liu, R. Sutarro, A. Tanaka, J. C. Cezar, N. B. Brookes, H. J. Lin, H. H. Hsieh, C. T. Chen, A. D. Rata, L. H. Tjeng, *Phys. Rev. X* **2016**, *6*, 041011.
- [20] A. Kalabukhov, R. Gunnarsson, J. Börjesson, E. Olsson, T. Claeson, D. Winkler, *Phys. Rev. B* **2007**, *75*, 121404.
- [21] I. C. Tung, G. Luo, J. H. Lee, S. H. Chang, J. Moyer, H. Hong, M. J. Bedzyk, H. Zhou, D. Morgan, D. D. Fong, J. W. Freeland, *Phys. Rev. Mater.* **2017**, *1*, 053404.
- [22] Z. Q. Liu, C. J. Li, W. M. Lü, X. H. Huang, Z. Huang, S. W. Zeng, X. P. Qiu, L. S. Huang, A. Annadi, J. S. Chen, J. M. D. Coey, T. Venkatesan, Ariando, *Phys. Rev. X* **2013**, *3*, 021010.
- [23] Y.-M. Kim, A. Morozovska, E. Eliseev, M. P. Oxley, R. Mishra, S. M. Selbach, T. Grande, S. T. Pantelides, S. V. Kalinin, A. Y. Borisevich, *Nat. Mater.* **2014**, *13*, 1019.
- [24] F. Y. Bruno, M. N. Grisolia, C. Visani, S. Valencia, M. Varela, R. Abrudan, J. Tornos, A. Rivera-Calzada, A. A. Ünal, S. J. Pennycook, Z. Sefrioui, C. Leon, J. E. Villegas, J. Santamaria, A. Barthélémy, M. Bibes, *Nat. Commun.* **2015**, *6*, 6306.
- [25] J. Rodríguez-Carvajal, M. Hennion, F. Moussa, A. H. Moudden, L. Pinsard, A. Revcolevschi, *Phys. Rev. B* **1998**, *57*, R3189.
- [26] G. Matsumoto, *J. Phys. Soc. Jpn.* **1970**, *29*, 606.
- [27] L. M. Zheng, X. Renshaw Wang, W. M. Lü, C. J. Li, T. R. Paudel, Z. Q. Liu, Z. Huang, S. W. Zeng, K. Han, Z. H. Chen, X. P. Qiu, M. S. Li, S. Yang, B. Yang, M. F. Chisholm, L. W. Martin, S. J. Pennycook, E. Y. Tsybmal, J. M. D. Coey, W. W. Cao, *Nat. Commun.* **2018**, *9*, 1897.
- [28] X. Hao, J. S. Moodera, R. Meservey, *Phys. Rev. B* **1990**, *42*, 8235.
- [29] D. Meng, H. Guo, Z. Cui, C. Ma, J. Zhao, J. Lu, H. Xu, Z. Wang, X. Hu, Z. Fu, R. Peng, J. Guo, X. Zhai, G. J. Brown, R. Knize, Y. Lu, *Proc. Natl. Acad. Sci. U S A* **2018**, *115*, 2873.
- [30] S. Matzen, J.-B. Moussy, P. Wei, C. Gatel, J. C. Cezar, M. A. Arrio, P. Saintcavit, J. S. Moodera, *Appl. Phys. Lett.* **2014**, *104*, 182404.
- [31] X. Renshaw Wang, C. J. Li, W. M. Lü, T. R. Paudel, D. P. Leusink, M. Hoek, N. Poccia, A. Vailionis, T. Venkatesan, J. M. D. Coey, E. Y. Tsybmal, Ariando, H. Hilgenkamp, *Science* **2015**, *349*, 716.
- [32] J. Töpfer, J. B. Goodenough, *J. Solid State Chem.* **1997**, *130*, 117.
- [33] Z. Marton, S. S. A. Seo, T. Egami, H. N. Lee, *J. Cryst. Growth* **2010**, *312*, 2923.
- [34] Y. Anahory, L. Embon, C. J. Li, S. Banerjee, A. Meltzer, H. R. Naren, A. Yakovenko, J. Cuppens, Y. Myasoedov, M. L. Rappaport, M. E. Huber, K. Michaeli, T. Venkatesan, Ariando, E. Zeldov, *Nat. Commun.* **2016**, *7*, 12566.
- [35] J. A. Alonso, M. J. Martínez-Lope, M. T. Casáis, A. Muñoz, *Solid State Commun.* **1997**, *102*, 7.
- [36] J. A. M. van Roosmalen, P. van Vlaanderen, E. H. P. Cordfunke, W. L. Ijdo, D. J. W. Ijdo, *J. Solid State Chem.* **1995**, *114*, 516.
- [37] K. Nakamura, K. Ogawa, *J. Solid State Chem.* **2002**, *163*, 65.
- [38] H. Lidbaum, J. Rusz, S. Rubino, A. Liebig, B. Hjörvarsson, P. M. Oppeneer, O. Eriksson, K. Leifer, *Ultramicroscopy* **2010**, *110*, 1380.
- [39] Z. L. Wang, J. S. Yin, Y. D. Jiang, J. Zhang, *Appl. Phys. Lett.* **1997**, *70*, 3362.
- [40] M. Varela, M. P. Oxley, W. Luo, J. Tao, M. Watanabe, A. R. Lupini, S. T. Pantelides, S. J. Pennycook, *Phys. Rev. B* **2009**, *79*, 085117.
- [41] Z. Chen, Z. Chen, Z. Q. Liu, M. E. Holtz, C. J. Li, X. R. Wang, W. M. Lü, M. Motapothula, L. S. Fan, J. A. Turcaud, L. R. Dedon, C. Frederick, R. J. Xu, R. Gao, A. T. N'Diaye, E. Arenholz, J. A. Mundy, T. Venkatesan, D. A. Muller, L. W. Wang, J. Liu, L. W. Martin, *Phys. Rev. Lett.* **2017**, *119*, 156801.
- [42] J. A. Mundy, Y. Hikita, T. Hidaka, T. Yajima, T. Higuchi, H. Y. Hwang, D. A. Muller, L. F. Kourkoutis, *Nat. Commun.* **2014**, *5*, 3464.
- [43] R. F. Egerton, *Ultramicroscopy* **2007**, *107*, 575.
- [44] H. Terashita, J. J. Neumeier, *Phys. Rev. B* **2005**, *71*, 134402.
- [45] P. Raychaudhuri, C. Mitra, P. D. A. Mann, S. Wirth, *J. Appl. Phys.* **2003**, *93*, 8328.
- [46] W.-j. Son, E. Cho, B. Lee, J. Lee, S. Han, *Phys. Rev. B* **2009**, *79*, 245411.
- [47] M. L. Reinle-Schmitt, C. Cancellieri, D. Li, D. Fontaine, M. Medarde, E. Pomjakushina, C. W. Schneider, S. Gariglio, P. Ghosez, J. M. Triscone, P. R. Willmott, *Nat. Commun.* **2012**, *3*, 932.
- [48] J. P. Perdew, A. Ruzsinszky, G. I. Csonka, O. A. Vydrov, G. E. Scuseria, L. A. Constantin, X. Zhou, K. Burke, *Phys. Rev. Lett.* **2008**, *100*, 136406.
- [49] G. Kresse, J. Furthmüller, *Comput. Mater. Sci.* **1996**, *6*, 15.
- [50] S. L. Dudarev, G. A. Botton, S. Y. Savrasov, C. J. Humphreys, A. P. Sutton, *Phys. Rev. B* **1998**, *57*, 1505.